Advanced Composites and Hybrid Materials (2021) 4:1398–1412
https://doi.org/10.1007/s42114-021-00304-2

ORIGINAL RESEARCH

Synthesis of 3D cerium oxide/porous carbon for enhanced electromagnetic wave absorption performance

Xinmeng Huang[1] · Xuehua Liu[1] · Zirui Jia[1,2,3] · Bingbing Wang[1] · Xiaomeng Wu[1] · Guanglei Wu[1]

Received: 16 April 2021 / Revised: 30 June 2021 / Accepted: 6 July 2021 / Published online: 31 July 2021

Abstract

A series of CeO_2/porous carbon composites are successfully prepared by hydrothermal method and subsequent pyrolysis method by using pine cone as biomass carbon source. Besides, the effect of cerium source on the electromagnetic (EM) parameters and electromagnetic wave (EMW) absorption performance of CeO_2/porous carbon composites is further investigated. Additionally, the possible EMW absorption mechanism is also discussed. The results show that the CeO_2/porous carbon composites show enhanced EMW absorption performance than pure porous carbon materials. Remarkably, with the cerium nitrate content of 0.6 mmol, the binary composites show a minimum reflection loss of − 56.04 dB with a thickness of 1.9 mm, and the effective absorption bandwidth is 5.28 GHz with a thickness of 2.1 mm. The remarkable electromagnetic wave absorbing property is attributed to the synergistic effect of porous carbon conductive framework and multiple interface polarization of heterointerfaces, as well as the oxygen vacancy defect caused by the unique structure of CeO_2. This work could provide inspiration to broaden the application of CeO_2 in dealing with the electromagnetic interference and pollution.

Keywords Porous carbon · Ceria · Oxygen vacancy · Dielectric loss · Electromagnetic wave absorption

1 Introduction

The rapid development of electronic information technology makes the application of electronic equipment more and more widely [1–4]. As a result, electromagnetic (EM) pollution has become an increasingly serious problem, which not only interferes with the use of satellite communication and communication equipment, but also endangers human health and safety [5, 6]. With the increasing demand for military safety and healthy life, electromagnetic wave (EMW) absorbing materials have attracted extensive attention. Electromagnetic absorbing material can convert electromagnetic energy into heat energy and other forms of energy [7–9]. However, the preparation of ideal EMW absorbing material with the characteristics of low weight, thin matching thickness, strong absorption capacity, and wide absorption bandwidth is still a challenge [10–13].

According to the absorbing mechanism, EMW absorbing materials are mainly divided into two categories: magnetic loss materials and dielectric loss materials. Among them, Fe_3O_4 [14], Co_3O_4 [15], and other magnetic loss materials are often limited due to their high density. In contrast, carbon fibers, carbon nanotubes, graphene oxide, porous carbon, and other carbon materials that belong to dielectric loss materials are considered ideal EMW absorbing candidates [16, 17]. Noticeably, porous carbon has attracted more and more attention due to its excellent electrical conductivity, large specific surface area, large pore size, and low density. Specifically, porous materials with nanopores or micropores can be considered effective media, which could be considered a mixture of solid and air. Hence, the existence of pore structure can reduce the dielectric constant and improve the impedance matching and make more EM waves enter the

Xinmeng Huang and Xuehua Liu contributed equally to this work.

✉ Zirui Jia
jiazirui@qdu.edu.cn

✉ Guanglei Wu
wuguanglei@qdu.edu.cn; wuguanglei@mail.xjtu.edu.cn

[1] State Key Laboratory of Bio-Fibers and Eco-Textiles, Institute of Materials for Energy and Environment, College of Materials Science and Engineering, Qingdao University, Qingdao 266071, People's Republic of China

[2] College of Chemistry and Chemical Engineering, Qingdao University, Shandong, Qingdao 266071, People's Republic of China

[3] Weihai Innovation Institute, Qingdao University, Qingdao 264200, Shandong, China

absorber [18–21]. At the same time, micropores increase the scattering and reflection of electromagnetic waves, which increases the transmission path of incident electromagnetic waves and provides more opportunities for the medium to attenuate EM wave energy. However, complex synthesis processes and certain environmental pollution limit the application of porous carbon materials. Therefore, it is necessary to investigate carbon materials with simple processes and environment-friendly and easily available raw materials [22–26].

In recent years, due to the rich source and environmental friendliness, biomass materials have attracted more attention [27–29]. According to previous studies, many biomass materials can be used to prepare porous carbon materials as EMW absorbing materials. For example, rice [30], eggshell membrane [31], walnut shells [32], and Spinach stem [33]. Through a simple carbonization process, biomass materials can be directly transformed into carbon materials [30]. In this paper, the porous carbon is synthesized by using pinecone as raw material, which is not only environmentally friendly but also low cost. The porous structure of carbon material is helpful to reduce its density and make the microwave absorbing material achieve the purpose of lightweight [34, 35]. However, according to previous reports, single-component carbon materials have high conductivity, which will lead to impedance mismatching. Besides, due to the dual loss mechanism, porous carbon materials are difficult to meet the requirements of wide bandwidth, lightweight, and thin thickness at the same time [36]. Therefore, the improvement of EMW absorption performance could be achieved by improving the impedance matching and the multiple loss of composites. Combining different materials with complementary characteristics to composite materials has become the research hotspot to prepare EMW absorbing materials [37–41].

Ceria is a common rare-earth compound, which is used in fuel cells, solar cells [42], photocatalysis [43], and other fields. Due to its poor electrical conductivity and high density, little research is about the application of CeO_2 on the EMW absorption field. However, with the advantages of good chemical stability, easy synthesis, low cost, and oxygen vacancy defects, CeO_2 shows huge potential in the field of EMW field. Previous studies have shown that the oxygen vacancy defects in CeO_2 crystal are mainly caused by the transformation from Ce^{4+} to Ce^{3+}, and with the increase of defects, the electrical conductivity and dielectric constant of CeO_2 increase obviously, which is conducive to the attenuation of incident EMW. It is reported that the chemical and physical properties of CeO_2 can be adjusted by recombination and doping, and the electronic structure can be optimized and the EMW absorption properties can be improved [44–46]. Therefore, it is feasible to synthesize multi-component composites composed of ceria for electromagnetic wave attenuation applications. For example, Wang et al. [47] prepared CeO_2 doped multi-walled carbon nanotubes hybrid materials by a hydrothermal method. The nanocomposites exhibited the minimum reflection loss (RL_{min}) of − 40.95 dB with a thickness of 3.5 mm. Li et al. [48] successfully synthesized a 3D accordion-like CeO_2/RGO composite by solvothermal and hydrothermal methods. The RL_{min} of the prepared material was − 50.6 dB with a thickness of 1.5 mm, and the effective absorption bandwidth (EAB) is 4.4 GHz; Li et al. [49] successfully synthesized 3D conductive network wrapped CeO_{2-x} Yolk@Shell hybrid microspheres by solvothermal method. The RL_{min} of composites was − 52.4 dB when the thickness was 4.0 mm and the EAB was 5.5 GHz. In addition, when the size of CeO_2 crystal is reduced to nanometer, the attenuation ability of electromagnetic wave will be enhanced due to quantum effect and interface effect. Therefore, ceria can be used as a candidate for EMW absorber [50].

However, the composite of porous carbon and ceria as electromagnetic wave absorbing material has not been reported. In this paper, CeO_2/porous carbon composites with three-dimensional structure were prepared by a hydrothermal method using porous carbon as the template. The relationship among morphology, structure, and EMW absorption performance of CeO_2/porous carbon composites was further investigated. In addition, the effects of CeO_2 content on the microstructure, EMW absorption performance, and EM parameters of the composites were studied. When the filler content is 20 wt%, the material shows excellent EMW absorption performance with the RL_{min} of − 56.04 dB when the thickness is 1.9 mm, and the EAB is 5.28 GHz at a thickness of 2.1 mm. Moreover, the EMW absorption mechanism of the composites was illustrated. The CeO_2/porous carbon composites prepared in this study have wide bandwidth, thin thickness, and excellent electromagnetic wave absorption performance, which is a candidate material for EMW absorption.

2 Experimental

2.1 Raw materials

The pinecone was obtained from the Pinus tabuliformis Carr in compass. Potassium hydroxide (KOH, 99.99%), cerium nitrate hexahydrate ($Ce(NO_3)_3$•$6H_2O$, 99.0%), NH_3•H_2O (25 wt%), and paraffin were bought from Aladdin, and anhydrous ethanol was purchased from Sinopharm Chemical Reagent Co., Ltd (Shanghai, China). All the chemical reagents were analytical grade and used without further purification. Water was the deionized water (DI, 18.25 MΩ).

2.2 Experiment section

2.2.1 Pretreatment of pinecone

First of all, the pinecone was cleaned with deionized water to remove impurities and dust on its surface. Then, the cleaned pinecone was dried at 80 °C. Finally, the pineal gland was cut as raw material.

2.2.2 Synthesis of porous carbon materials

Firstly, the homogeneous solution was obtained by dissolving 2 g KOH in 30 mL deionized water. Then, 2 g pinecones were added into the solution and treated with ultrasonic for 30 min to make the pinecone fully soaked. Then, the pinecone was dried at 80 °C overnight. The dried pinecone was carbonized in an Ar flow tubular furnace at 650 °C for 1 h with a heating rate of 2 °C/min. After cooling to room temperature naturally, the intermediate products were ground into powder in an agate mortar. The by-product and excess KOH were removed by deionized water, and the final sample was obtained after drying at 80 °C. The porous carbon materials were named as S0.

2.2.3 Synthesis of CeO_2/porous carbon composites

Typically, 200 mg synthesized porous carbon was dispersed into 60 mL deionized water under continuous stirring for 10 min. Then, a certain amount of cerium nitrate hexahydrate was dispersed in the uniform solution under magnetic stirring until completely dissolved. The $NH_3{\cdot}H_2O$ (25 wt%) was gradually added to the solution until the pH value became 11. Then, the system was transferred into a Teflon-lined autoclave at 160 °C for 12 h. After cooling down to room temperature naturally, the prepared samples were washed with deionized water and ethanol and dried overnight at 80 °C. After drying, the final sample was obtained after heat-treatment at 500 °C for 1 h under Ar atmosphere (heating rate 2 °C/min). As-prepared composites were named by the additional amount of $Ce(NO_3)_3{\bullet}6H_2O$ as S1 (0.2 mmol), S2 (0.4 mmol), S3 (0.6 mmol), S4 (0.8 mmol), and S5 (1.0 mmol), respectively.

2.3 Characterization

The crystalline structure of samples was determined by powder X-ray diffraction (Rigaku Ultima IV with Cu–Ka radiation ($\lambda = 0.15418$)). The Raman spectra of samples were collected by using a Renishaw inVia Plus Micro-Raman spectroscopy system equipped with a 50-mW DPSS laser at 532 mm. The FTIR spectrum was recorded on PerkinElmer, and Spectrum 100 was selected to study the surface structure of the sample. The thermogravimetric analysis (TGA) was carried out from room temperature to 800 °C on an SDT Q600 analyzer with a heating rate of 10 °C/min. The stage of elements in the surface of composites was characterized by X-ray photoelectron spectroscopy (XPS) on Thermo Fisher ESCALAB 250 Xi spectrometer with an Al Ka X-ray source (1486.6 eV). The morphology and element mapping of samples were obtained by field emission scanning electron microscope (SEM, JEOL JSM-7800 F), and lattice spacing was observed on transmission electron microscope (TEM, JEOL JEM-2100).

2.4 Electromagnetic parameter measurement

The composites were pressed into a toroidal-shaped pipe by mixing with the paraffin. The height, outer diameter, and inner diameter of the pipe were about 2.00 mm, 7.00 mm, and 3.04 mm, respectively. The weight ratio of composites to paraffin was 1:4. Based on the coaxial-line method, the electromagnetic parameters (ε_r and μ_r) of composites were obtained on a vector network analyzer (VNA, Agilent N5222A). The reflection loss (RL) values of composites in the frequency from 2 to 18 GHz at 0.1–10 mm were worked out by transmission line theory as follows [51–54]:

$$Z_{\text{in}} = Z_0\sqrt{\frac{\mu_r}{\varepsilon_r}}\tanh\left|j\left(\frac{2\pi fd}{c}\right)\sqrt{\varepsilon_r\mu_r}\right| \tag{1}$$

$$\text{RL}(dB) = 20\log\left|\frac{Z_{\text{in}} - Z_0}{Z_{\text{in}} + Z_0}\right| \tag{2}$$

where ε_r and μ_r are the complex permittivity and permeability, f is the frequency, d is the thickness of the sample, c is the light speed in a vacuum, and Z_{in} and Z_0 are the input impedance and free space impedance, respectively. When the RL value lower than − 10 dB, it means that more than 90% EM waves would be absorbed and consumed by the absorber.

3 Results and discussion

The crystal structures of S0 to S5 are recorded by XRD. Figure 1b displays that the X-ray diffraction peaks at $2\theta = 28.5°$, 33.1°, 47.5°, 56.3°, 69.4°, 76.7°, and 79.1° are consistent with the (111), (200), (220), (311), (400), (331), and (420) crystal planes of cubic fluorite CeO_2, indicating that CeO_2 is successfully anchored onto porous carbon [55]. However, the diffraction peaks of porous carbon are difficult to distinguish in S1 to S5. This phenomenon occurs because porous carbon is amorphous and has no obvious diffraction peak, which can be confirmed by TEM.

The graphitization degree of S0–S5 is detected by Raman spectroscopy. Figure 1c shows that two typical peaks of CeO_2/porous carbon composites located at around

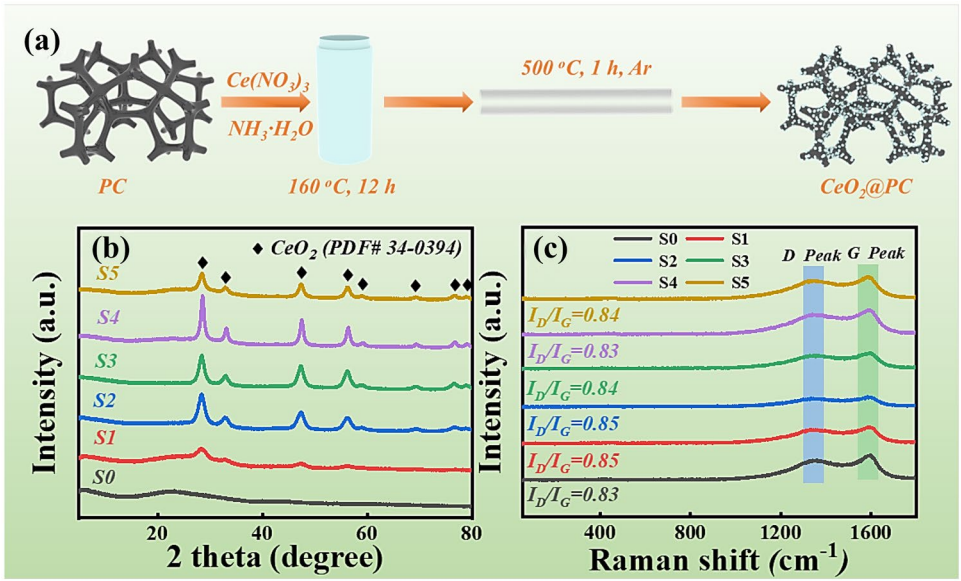

Fig. 1 (**a**) Schematic illustration of the synthesis process of CeO_2/porous carbon composites. (**b**) XRD patterns of the samples of S0–S5. (**c**) Raman spectra of the samples of S0–S5

1350 cm^{-1} and 1580 cm^{-1} can be assigned to the D and G bands. Generally, the D band represents the defects, limited size crystal, or disorder of graphite, while the G band is the in-plane vibration of sp^2 C atom, which represents the ordered structure of graphite carbon [56]. Therefore, the degree of graphitization can be reflected by the intensity ratio of D peak to G peak (I_D/I_G). By comparing the I_D/I_G value of S0–S5, it is found that the graphitization degree of the samples shows little change after adding ceria, indicating that ceria addition has little effect on the graphitization degree of the samples.

The molecular structures of the C, O, and Ce elements are characterized by FT-IR. As is shown in Fig. 2a, the absorption peak at 3435 cm^{-1} corresponds to the O–H group in H_2O, which is adsorbed on the sample surface. While the absorption peak at 2360 cm^{-1} comes from C = O. In addition, the absorption peak at 1623 cm^{-1} could confirm the existence of O–C = O, the absorption peak at 1100 cm^{-1} is C–O. According to previous studies, the presence of oxygen-containing groups will cause the charge asymmetric distributions, inducing the formation of dipoles. These dipoles could rotate toward the alternating electromagnetic field, converting electromagnetic energy to thermal energy through relaxation loss, which increases the ability to consume the energy of electromagnetic waves.

The content of CeO_2 in S1–S5 samples is determined by thermogravimetric analysis (TGA). As depicted in Fig. 2b, the thermal decomposition of S1–S5 is mainly divided into

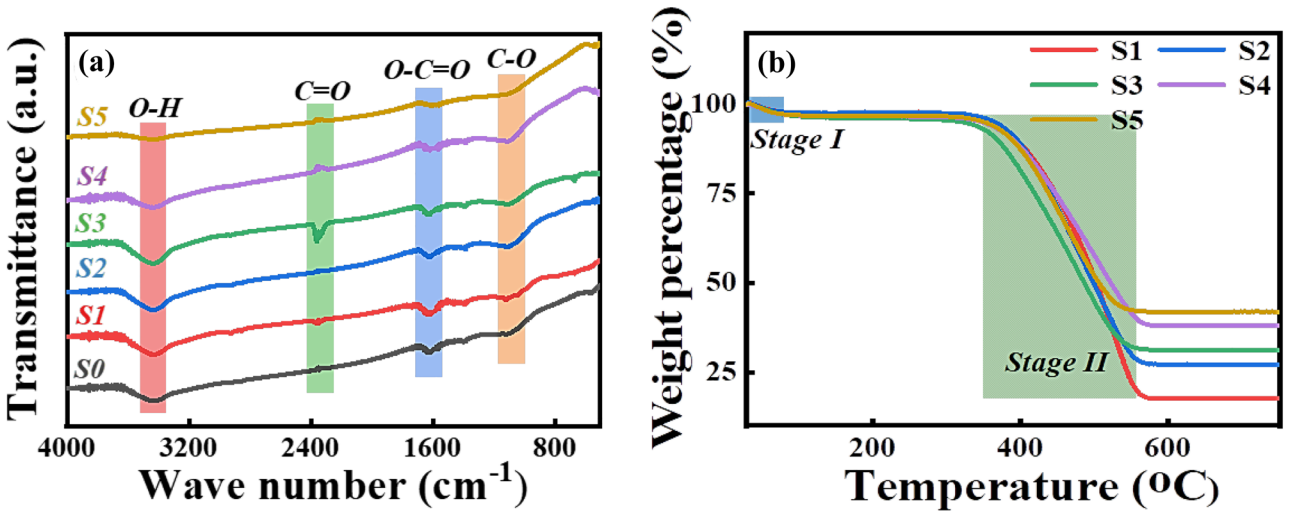

Fig. 2 (**a**) FT-IR of S0-S5. (**b**) TGA of S0–S5

two stages. Firstly, a little weight loss (~4 wt%) is caused by the loss of water adsorbed on the sample surface below 100 °C, corresponding to the O–H bond in the FT-IR. Secondly, in the range of 350 to 580 °C, all the samples have obvious weight loss, which may be ascribed to the decomposition of porous carbon in the air. Then, the proportion of CeO_2 was deduced from the residual products. Therefore, the contents of CeO_2 in S1–S5 are estimated as 17.5 wt%, 26.9 wt%, 31.2 wt%, 37.8 wt%, and 41.9 wt% respectively. With the increase of molar amount of cerium salt, the proportion of cerium dioxide in the sample is increasing. The XRD of the residue of composites is shown in Fig. S1 (Supporting Information), which shows the CeO_2 phase.

The surface chemical composition and valence state are analyzed by XPS. According to Fig. 3a, the presence of C, O, and Ce elements is confirmed. Figure 3b illustrates the groups corresponding to C–C/C=C, C–O, C=O, and O–C=O at 284.2, 285.1, 286.0, and 289.0 eV in the C 1 s peak, respectively [45]. Figure 3c shows that groups corresponding to Ce–O, O–H, and O^{2-} at 529.3, 531.2, and 532.1 eV in the O 1 s peak [57]. Figure 3d depicts the Ce 3d spectrum. Ce^{4+} in CeO_2 is labeled as U, U″, U‴, V, V″, and V‴, and Ce^{3+} in CeO_2 is labeled as V′ and U′ [45]. Therefore, the existence of Ce^{4+} and Ce^{3+} in the Ce 3d spectrum of S3 indicates the existence of oxygen vacancies [57]. Specifically, oxygen vacancies are generated to compensate for the negative charge generated by the increase of Ce^{3+} in CeO_2. When the oxygen vacancy increases, the electrical conductivity increases, booming the conduction loss [58].

Figure 4 shows the surface morphology, structure, and element diagram of the samples. Figure 4(a1 and a2) depict the morphology and structure of porous carbon material, which is a three-dimensional porous framework with pore structure distributed on its surface. As is shown in Fig. 4(b1–f2), compared with the pure porous carbon material, the CeO_2/porous carbon composites could show that CeO_2 nanoparticles are anchored on the porous carbon material clearly. Figure 4(b1–f2) illustrate that, with the increase of CeO_2 content in the sample, from CeO_2 nanoparticles cannot completely wrap the porous carbon to uniformly wrap the porous carbon, and then, CeO_2 nanoparticles are closely packed and gathered on the porous carbon material. As is shown in Fig. 4g, the O and Ce were uniformly distributed on the outer surface of S3, which further verifies the existence of CeO_2 nanoparticles on porous carbon.

Figure 5a and b show that the porous carbon is amorphous, which is the same as the conclusion obtained by XRD. As is shown in Fig. 5c, the porous carbon and CeO_2 nanoparticles are closely combined to form a nanoscale heterogeneous interface. Figure 5d shows that the size of

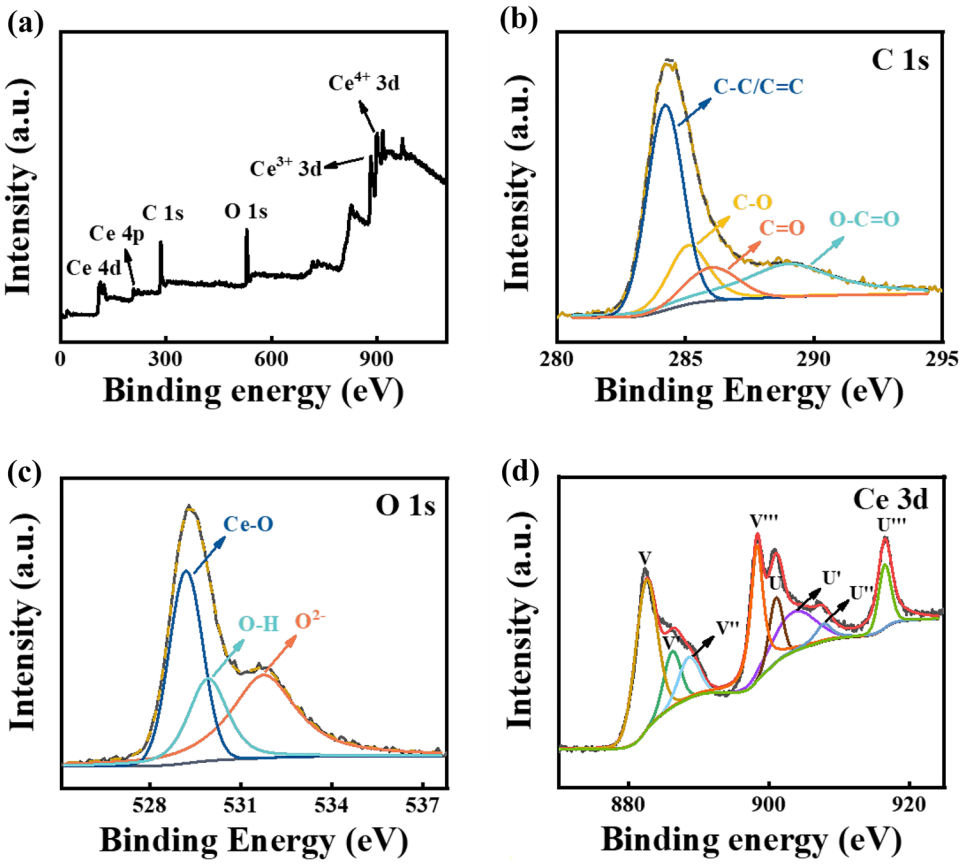

Fig. 3 (**a**) Full XPS spectrum and high-resolution. (**b**) C 1 s. (**c**) O 1 s. (**d**) Ce 3d

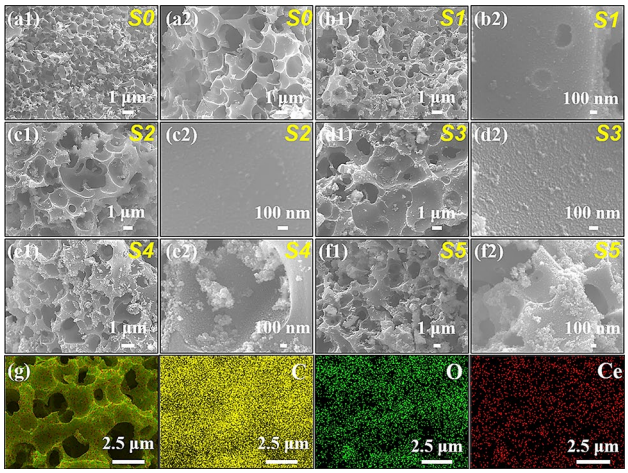

Fig. 4 (**a**–**f**) SEM images of S0–S5. (**g**) Elements mapping of a selected area of S3

CeO_2 nanoparticles was about 6–10 nm, and the CeO_2 nanoparticles were uniformly anchored on the surface of porous carbon. As is shown in Fig. 5e, the crystal plane spacing of 0.27 and 0.31 nm corresponds to the (200) and (111) crystal plane of CeO_2, which is consistent with the XRD spectrum. Figure 5f depicts the selected-area electron diffraction image of composites. Four diffraction rings correspond to (311), (111), (220), and (200) crystal planes of CeO_2. From the above observation, it could be indicated that the CeO_2/porous carbon composites are successfully synthesized.

The value of reflection loss (RL) is a key indicator to evaluate EMW absorption performance. In addition, when the RL value is less than − 10 dB, the EM absorber can absorb more than 90% of the electromagnetic wave. Figure 6 shows the 3D reflection loss of pure porous carbon and CeO_2/porous carbon composites with different loadings. From Fig. 6a, the minimum RL value (RL_{min}) of S0 is − 22.24 dB at the thickness of 3.1 mm, confirming poor EMW absorption performance. Figure 6b shows that, after decorating porous carbon with CeO_2 nanoparticles, S1 exhibits much better EMW absorption performance with RL_{min} of − 67.05 dB at a thickness of 4.4 mm than that of S0, and the S2 shows the RL_{min} of − 53.68 dB when the thickness is 3.4 mm. As for the S3, the RL_{min} is up to − 56.04 dB when the thickness is 1.9 mm, the RL_{min} of S4 dropped to − 51.04 dB with a thickness of 5.2 mm, and the S5 shows the RL_{min} of − 35.56 dB at the matching thickness increase of 9.4 mm. According to Fig. 6a–f, with the increasing proportion of CeO_2 in composites, the RL_{min} of the samples shows an increasing process with the thickness decreases. Consequently, it could be found that the S3 shows the optimal absorption performance among as-obtained composites.

Figure 7a–f show the effective absorption bandwidth (EAB) of S0–S5. From Fig. 7a–f, S1, S2, and S3 possess wide bandwidth with thin matching thickness. However, S0, S4, and S5 show a relatively thick thickness when the maximum EAB is obtained. Specifically, when the thickness of S1 is 2.0 mm, the EAB is 5.52 GHz. The bandwidth of S2 and S3 is 5.04 GHz and 5.28 GHz, respectively.

The complex permittivity ($\varepsilon_r = \varepsilon' - j\varepsilon''$) and complex permeability ($\mu_r = \mu' - j\mu''$) of composites are measured. As is shown in Fig. 8a, the ε' value of S0–S4 decreases with the increase of frequency, which is called dispersion behavior [59]. However, the ε' of S5 remains at a stable value of 6 and that is lower than that of S0–S4, implying poor dielectric loss ability. As is shown in Fig. 8b, when the frequency increases, the ε curve of samples firstly shows a downward trend, and multiple relaxation peaks appear with the increase of frequency, which indicates the existence of dielectric loss behavior. From the previous reports, the dielectric loss could be divided into polarization loss and conductive loss [60]. Generally speaking, electron polarization and ion polarization can be excluded, because they usually occur in the THz and PHz ranges. Then, as the frequency continues to increase, the ε values of S0–S5 show an increasing trend, which means that, when the frequency of EMW increases, the dipole can quickly reorient and respond to the external electric field,

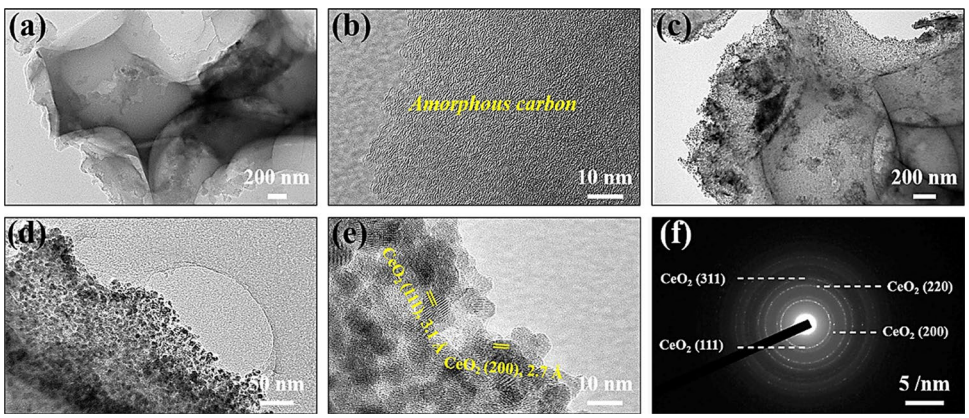

Fig. 5 (**a**) TEM, (**b**) HR-TEM images of S0, (**c**) TEM, (**d**–**e**) HR-TEM images, and (**f**) SAED patterns of S3

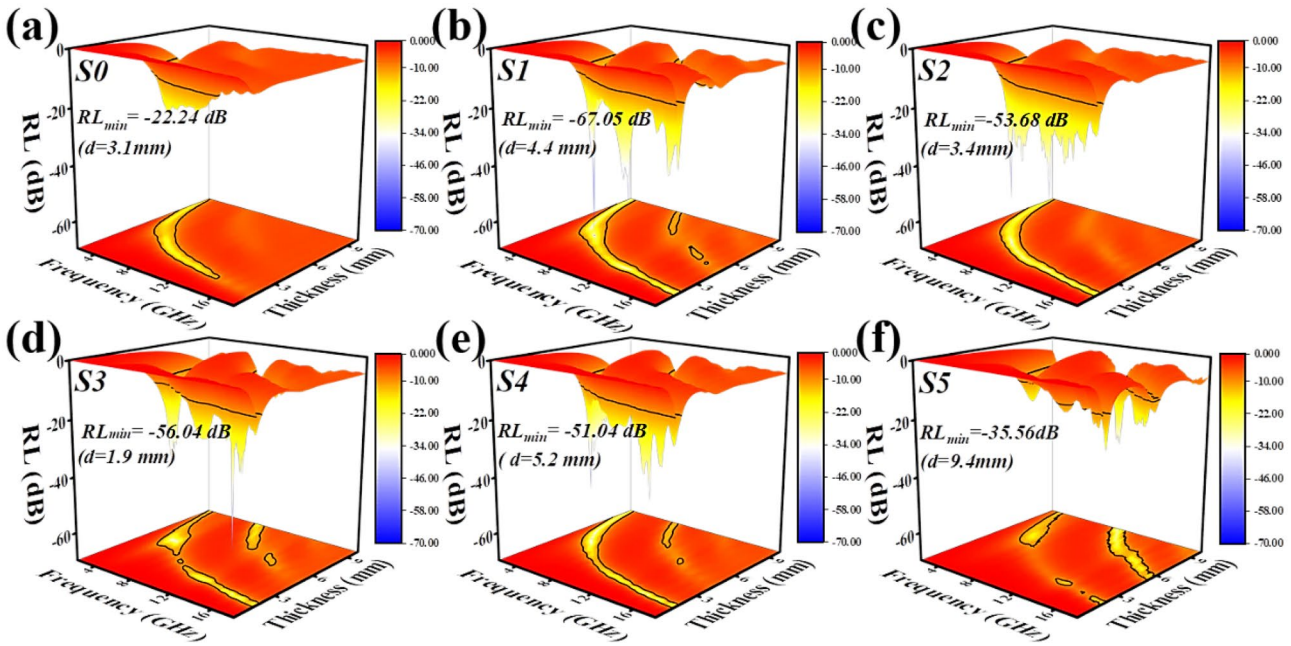

Fig. 6 Reflection Loss in the frequency of 2–18 GHz for the S0 (**a**), S1 (**b**), S2 (**c**), S3 (**d**), S4 (**e**), and S5 (**f**), respectively

which means that the effect of dipole polarization is also very small. In this case, multiple interfaces between CeO_2 and porous carbon, CeO_2 and CeO_2, CeO_2, and paraffin lead to interfacial polarization. In addition, porous carbon can provide a conductive path for the transmission of electrons. Based on the free-electron theory [58]:

$$\varepsilon'' = 1/2\varepsilon_0\pi\rho f \tag{3}$$

where ε_0, ρ, and f are permittivity of the vacuum, resistivity, and frequency of the EMW, respectively. As is shown in Fig. 8b, the maximum value of ε'' of S0 is mainly caused by the high electrical conductivity of porous carbon, which will

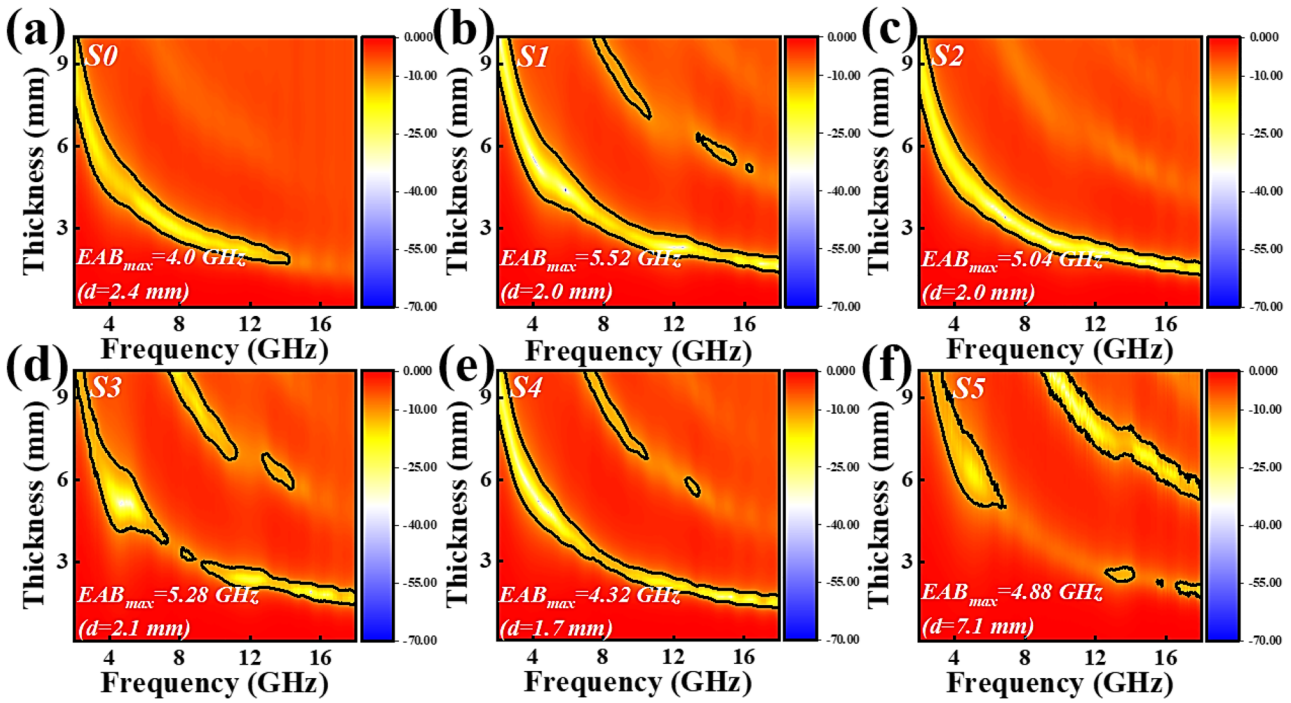

Fig. 7 Contour map of absolute values of S0 (**a**), S1 (**b**), S2 (**c**), S3 (**d**), S4 (**e**), and S5 (**f**)

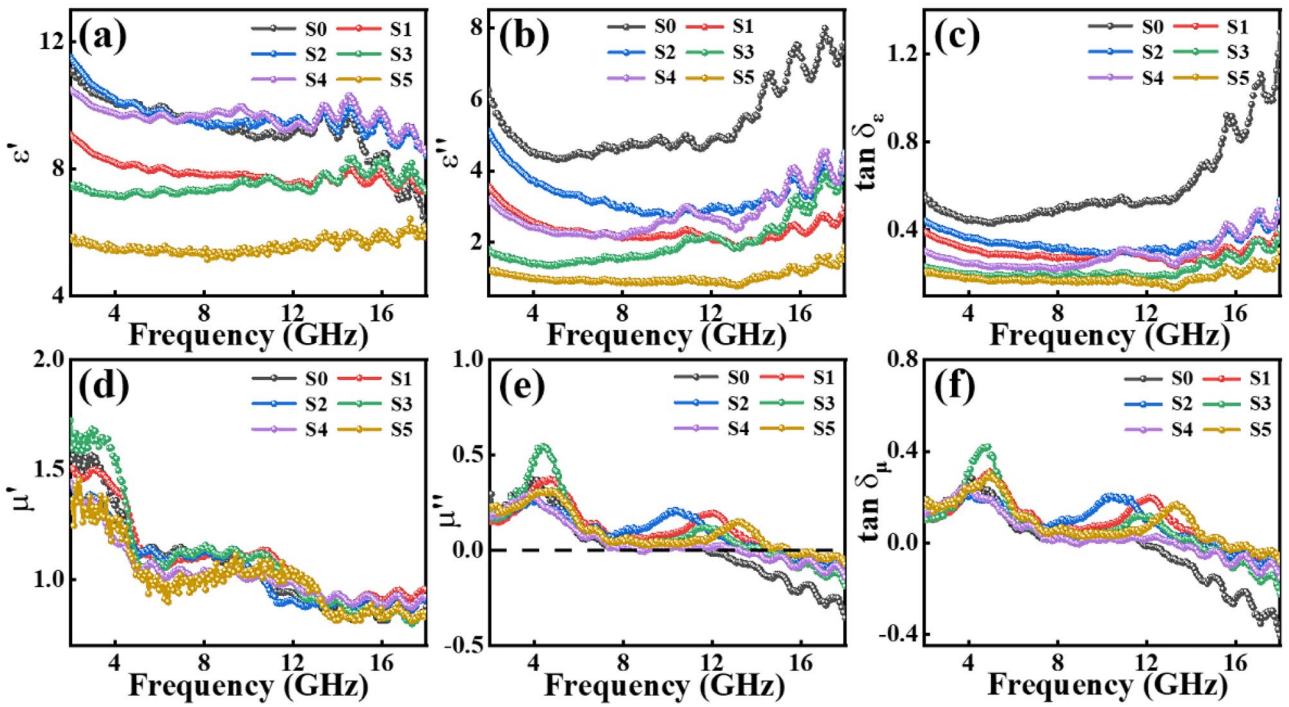

Fig. 8 (**a**) Real part and (**b**) imaginary part of complex permittivity of S0–S5. (**c**) Dielectric loss tangent of S0–S5, (**d**) real part, and (**e**) imaginary part of complex permeability of S0-S5. (**f**) Magnetic loss tangent of S0–S5

cause poor impedance matching and cause EM waves to be reflected from the absorber interface rather than absorbed, resulting in poor performance.

$\tan\delta_E$ represents the dielectric loss capacity of the sample [60]. As is shown in Fig. 8c, the $\tan\delta_E$ value of S0 shows more obvious fluctuation than that of S1–S5 at 2–18 GHz, and the $\tan\delta_E$ value of S1–S5 tends to be a constant and less than S0. The explanation of this phenomenon can be found in some previous studies; pure porous carbon will have enough charge to reverse the traditional dielectric behavior under external electromagnetic wave. In this case, the conductive loss is dominant in the dielectric loss. When porous carbon is modified with CeO_2, the interface between CeO_2 and porous carbon polarizes and accumulates a lot of charges. When the ceria content reaches a higher level, the insulating properties of CeO_2 will hinder this process, resulting in relatively poor dielectric properties. Therefore, the $\tan\delta_E$ value of S1–S5 is lower than that of S0. The trends of $\tan\delta_\mu$ and μ'' of all samples are similar with the increase of frequency. According to Fig. 8c and f, by comparing $\tan\delta_E$ and $\tan\delta_\mu$, the dielectric loss and magnetic loss both play an important role in EM loss.

The impedance matching diagram of S0–S5 is shown in Fig. 9. The impedance value ($Z = Z_{in}/Z_0$) is calculated as 0.1–10 mm at 2–18 GHz. The calculation formula is as follows [51–54]:

$$Z = \frac{Z_{in}}{Z_0} = \sqrt{\frac{\mu_r}{\varepsilon_r}}\tanh\left|j\left(\frac{2\pi fd}{c}\right)\sqrt{\varepsilon_r\mu_r}\right| \tag{4}$$

As is shown in Fig. 9, the area between 0.9 and 1.1 is drawn with black lines, and the impedance matching degree of the samples can be expressed by calculating the area between the two black lines. Large area proves good impedance matching. It can be inferred that S3 has the best impedance matching, which is consistent with the conclusion that S3 shows the best absorbing performance.

Generally speaking, dielectric conductivity is an important index that affects the response of EMW absorbing materials to EM field. The dielectric conductivity could be expressed by the following formulate [61]:

$$\sigma = \omega\varepsilon_0\varepsilon'' \tag{5}$$

where ω ($\omega = 2\pi f$) is the angular frequency, ε_0 ($\varepsilon_0 = 8.854\times10^{-12}$ F/m) represents the permittivity of free space, and ε'' is the imaginary of complex permittivity. The dielectric conductivity of S0–S5 is shown in Fig. 10a. The S0 shows the maximum dielectric conductivity, which means that the influence of its conductive loss on the electromagnetic wave attenuation is more apparent in as-obtained samples. However, high dielectric conductivity will cause impedance mismatch, which leads to more electromagnetic

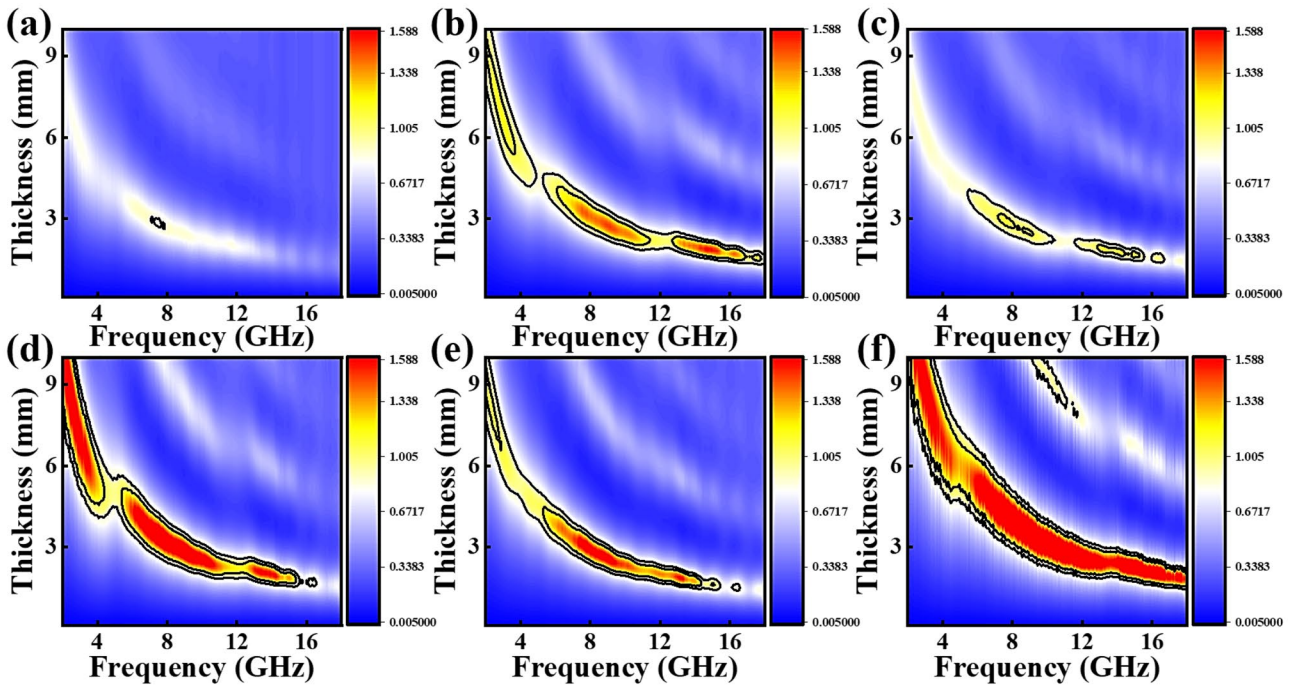

Fig. 9 Normalized input impendence (Z_{in}/Z_0) of S0 (**a**), S1 (**b**), S2 (**c**), S3 (**d**), S4 (**e**), and S5 (**f**)

waves reflected from the surface of the absorber rather than absorbed.

In addition to the impedance matching index, the attenuation constant α is also a key indicator, which reflects the attenuation ability of the S0–S5. The α can be expressed as [62–64]:

$$\alpha = \frac{\sqrt{2}\pi f}{c} \times \sqrt{(\mu''\varepsilon'' - \mu'\varepsilon') + \sqrt{(\mu'\varepsilon'' + \mu''\varepsilon')^2 + (\mu''\varepsilon'' - \mu'\varepsilon')^2}} \tag{6}$$

Figure 10b displays the α values of S0–S5. The S5 has the lowest α value and the worst performance. It is worth noting that S0 and S4 have higher α value, but they show poor electromagnetic wave absorption performance. On the contrary, S3 with low attenuation constant has the best absorption performance. This phenomenon could be explained that the impedance matching value of S3 is higher than that of S0 and S4, which indicates that more EMW can enter S3 and have more chances to be attenuated. Therefore, compared with the attenuation constant, the impedance matching is the main factor affecting the EMW absorption performance.

According to the Debye theory, the ε' and ε'' could be calculated by the following formula [65, 66]:

$$\varepsilon' = \varepsilon_\infty + \frac{\varepsilon_s - \varepsilon_\infty}{1 + (2\pi f)^2 \tau^2} \tag{7}$$

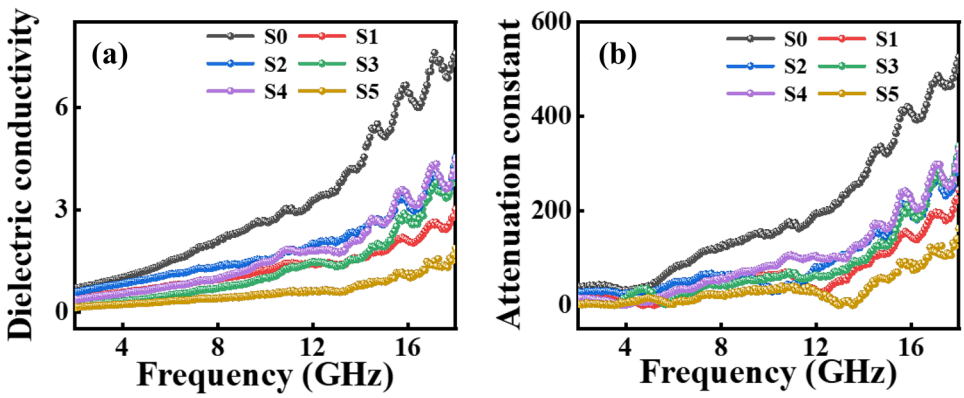

Fig. 10 (**a**) Dielectric conductivity of S0–S5. (**b**) Attenuation constants of S0–S5

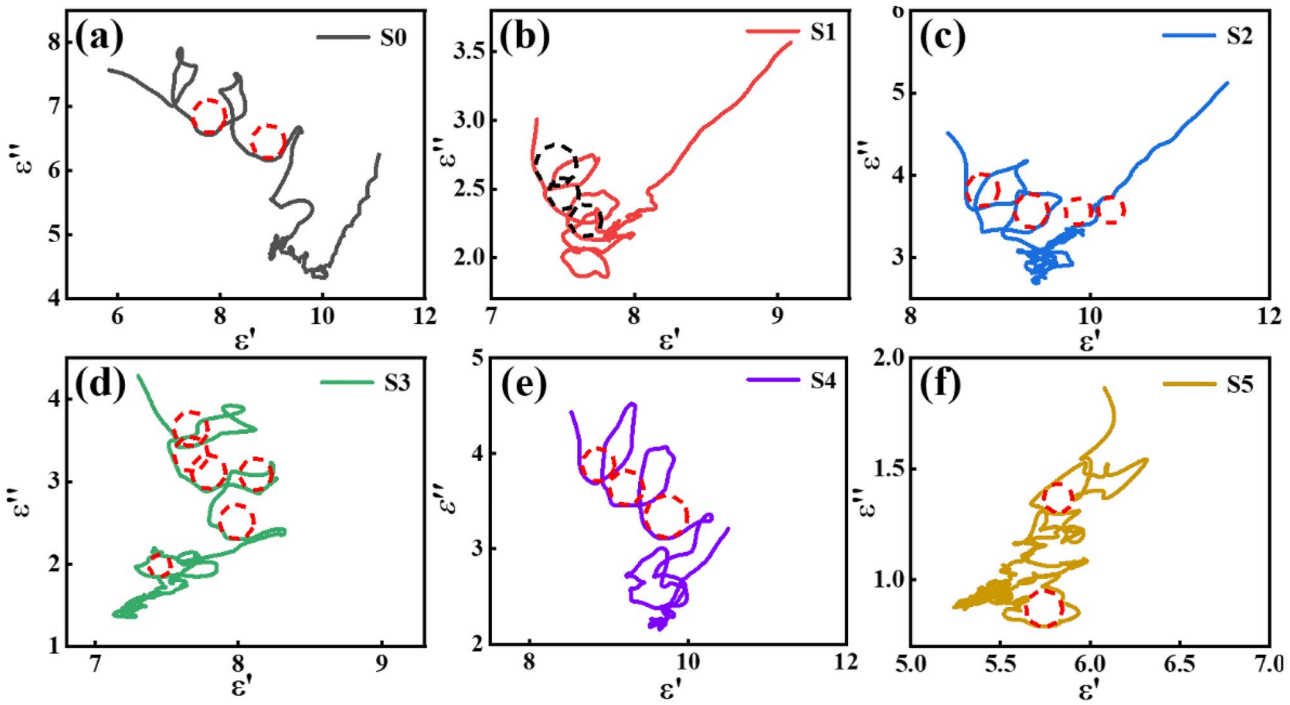

Fig. 11 Cole–Cole semicircle curves of S0 (**a**), S1 (**b**), S2 (**c**), S3 (**d**), S4 (**e**), and S5 (**f**)

$$\varepsilon'' = \frac{2\pi f\tau(\varepsilon_s - \varepsilon_\infty)}{1 + (2\pi f)^2\tau^2} \tag{8}$$

where the ε_s represents the static dielectric constant, ε_∞ represents the optimal dielectric constant, f represents the matching frequency, and τ is the polarization relaxation

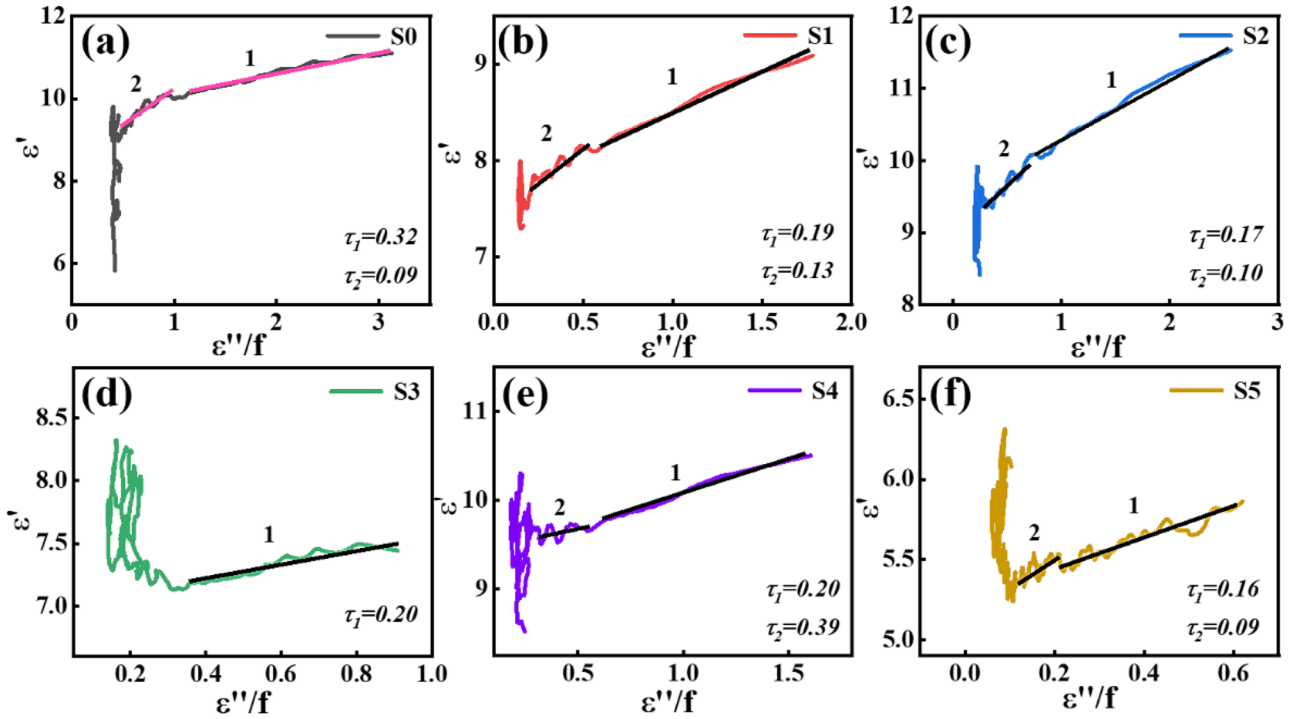

Fig. 12 The relationship between ε' and ε''/f of S0 (**a**), S1 (**b**), S2 (**c**), S3 (**d**), S4 (**e**), and S5 (**f**)

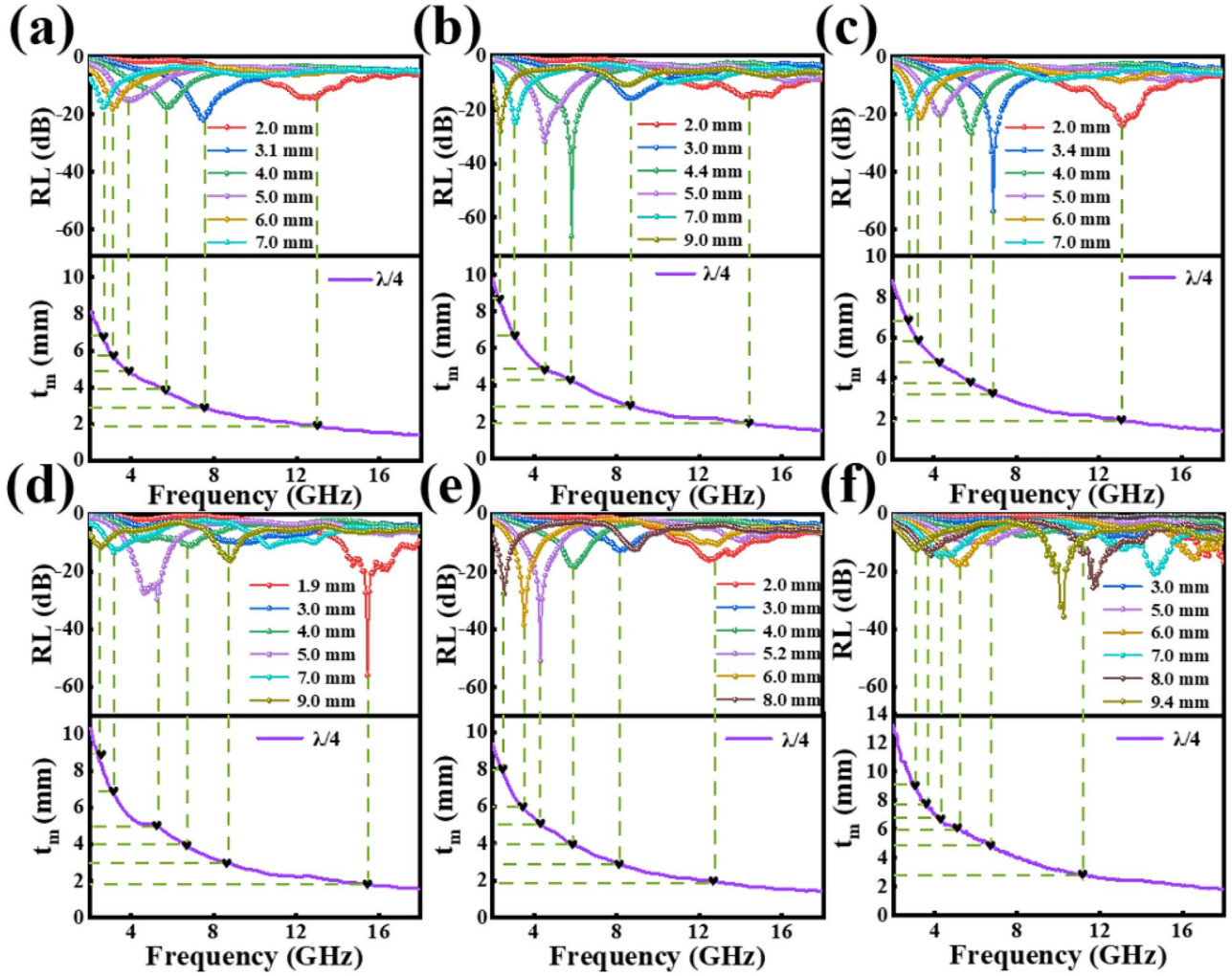

Fig. 13 Dependence of matching thickness (t_m) on matching frequency (f_m) of S0–S5 at a wavelength of $\lambda/4$

time. Therefore, the Cole–Cole equation could be expressed by the following formula [65, 66]:

$$(\varepsilon' - \frac{\varepsilon_s + \varepsilon_\infty}{2})^2 + (\varepsilon'')^2 = (\frac{\varepsilon_s - \varepsilon_\infty}{2})^2 \quad (9)$$

Figure 11 shows the Cole–Cole semicircles of the samples with different CeO_2 loadings. Figure 11a–c present that the Cole–Cole curves in these three images show similar trends, with several Cole–Cole semicircles and an upward long tail. Through previous studies, the upward long tail indicates the conduction loss in S0–S2, and the Cole–Cole semicircle indicates the existence of polarization relaxation in S0–S5. According to the Cole–Cole semicircle curves, S3 processes the most Cole–Cole semicircles, which means that outstanding polarization relaxation occurs in S3.

Based on Eqs. (7) and (8), the ε' could be expressed as follows [67]:

$$\varepsilon' = \frac{1}{2\pi\tau}\frac{\varepsilon''}{f} + \varepsilon_\infty \quad (10)$$

Theoretically, if the dielectric loss is related to the polarization relaxation, the functional relationship between ε' and ε''/f will be linear. The relaxation time is expressed by the slope of the linear function. The fitting lines are obtained by means of linear regression method, and the relaxation time is obtained by calculation. The relaxation time can be calculated by the formula [67]:

$$\tau = \frac{1}{2\pi k} \quad (11)$$

where the k is the slope of the linear function. Figure 12 shows the functional relationship between ε' and ε''/f of S0–S5. As is shown in Fig. 12, not all curves fit into a single straight line, which means that the multiple polarization relaxation process. Based on the previous reports, this

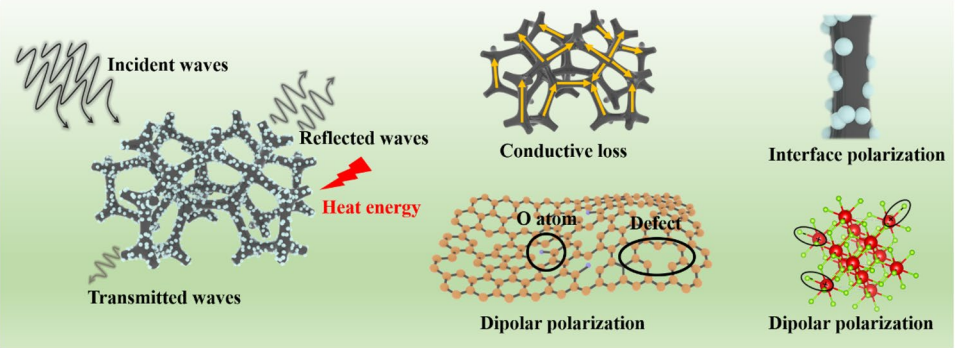

Scheme 1 Schematic illustration of the electromagnetic wave absorption performance of composites

phenomenon could be explicated as follows: (1) the dipoles are not all in the same environment. Therefore, the response of dipoles to EM field is distinct. Hence, the as-obtained samples showed different slopes. (2) Different polarization processes possess various relaxation time and provide different contributions to the dielectric loss.

The matching thickness (t_m) and absorption peak frequency (f_m) are two key factors affecting the application of EMW absorber. According to the quarter-wavelength matching theory, the relationship between t_m and f_m is as follows [68–70]:

$$t_m = \frac{n\lambda}{4} = \frac{nc}{4f_m\sqrt{|\mu_r||\varepsilon_r|}}(n = 1,3,5\ldots) \tag{12}$$

where t_m and f_m represent the matching thickness and the frequency of the RL_{min} value, c is the light speed in free space. $|\mu_r|$ and $|\varepsilon_r|$ are the modulus of the μ_r and ε_r, respectively. From Fig. 13, with the increase of matching thickness, the reflection loss peak of S0–S5 gradually moves to low frequency. The black hearts are the best matching thickness obtained from the RL diagram, and the purple line is calculated from the above equation. In Fig. 13, the black hearts are almost on the purple line. The results show that the quarter-wavelength theory can explain the EMW absorption characteristics of S0–S5.

The electromagnetic wave absorption mechanism of CeO_2/porous carbon composites can be summarized as shown in Scheme 1. Firstly, the porous structure could be regarded as the solid-air composites, which improves the impedance matching and electromagnetic wave absorption capacity. Moreover, the porous carbon framework forms a conductive network to improve the conductive loss and O atom defects on porous carbon can act as dipoles to enhance the attenuation of electromagnetic waves. Secondly, the introduction of CeO_2 nanoparticles into the porous carbon structure produces rich interfaces (such as CeO_2–CeO_2, CeO_2-porous carbon). The interface polarization generated by the heterogeneous interface and the conductive loss generated by the conductive network of porous carbon has a synergistic effect, which transforms the EMW energy into heat and other forms of energy. Thirdly, multiple reflection scattering increases the dissipation of electromagnetic wave. Moreover, Ce^{4+} transforms into Ce^{3+} in CeO_2 to produce a large number of oxygen vacancies, which can be used as dipoles, which is conducive to electron migration, enhanced charge relaxation, and increased electromagnetic wave attenuation. All the loss mechanisms mentioned work together to attenuate incident EMW energy.

4 Conclusions

In summary, CeO_2/porous carbon composites were successfully fabricated by a simple hydrothermal method and subsequent pyrolysis method. Porous carbon materials were prepared by using pinecone as the precursor, and then, CeO_2 nanoparticles were anchored on the surface of porous carbon by subsequent hydrothermal and pyrolysis methods. In addition, the effects of cerium addition on the morphology, EM parameters, and EMW absorption performance of all the samples were also studied. Through the characterization, it can be concluded that, when the cerium salt content is 0.6 mmol, the RL_{min} of − 56.04 dB is obtained with a thickness of 1.9 mm, and the EAB is 5.28 GHz with a thickness of 2.1 mm. Multiple interface polarization along with conductive loss and dipolar polarization is contributed to excellent electromagnetic wave absorption performance of the CeO_2/porous carbon composites and multiple reflection and scattering enhance the dissipation of electromagnetic waves. Therefore, the as-obtained composites can be regarded as a potential candidate absorber to deal with the electromagnetic interference and pollution.

Supplementary Information The online version contains supplementary material available at https://doi.org/10.1007/s42114-021-00304-2.

Acknowledgements The authors acknowledge the support from The Thousand Talents Plan, The World-Class University and Discipline, The Taishan Scholar's Advantageous and Distinctive Discipline

Program of Shandong Province, and The World-Class Discipline Program of Shandong Province.

Funding This work was financially supported by the National Natural Science Foundation of China (No. 51407134), Natural Science Foundation of Shandong Province (No. ZR2019YQ24), Shandong Taishan Scholars Young Expert Program (No. tsqn202103057), China Postdoctoral Science Foundation (No. 2016M590619), and the Qingchuang Talents Induction Program of Shandong Higher Education Institution (Research and Innovation Team of Structural–Functional Polymer Composites).

Declarations

Conflict of interest The authors declare no competing interests.

References

1. Hou TQ, Jia ZR, Feng AL, Zhou ZH, Liu XH, Lv HL, Wu GL (2021) Hierarchical composite of biomass derived magnetic carbon framework and phytic acid doped polyanilne with prominent electromagnetic wave absorption capacity. J Mater Sci Technol 68:61–69
2. Zhou XM, Fu QG, Liu H, Gu HB, Guo ZH (2021) Solvent-free nanoalumina loaded nanocellulose aerogel for efficient oil and organic solvent adsorption. J Colloid Inter Sci 581:299–306
3. Zhang HX, Jia ZR, Feng AL, Zhou ZH, Zhang CH, Wang KK, Liu N, Wu GL (2020) Enhanced microwave absorption performance of sulfur-doped hollow carbon microspheres with mesoporous shell as a broadband absorber. Compos Commun 19:42–50
4. Lv HL, Yang ZH, Ong SJH, Wei C, Liao HB, Xi SB, Du YH, Ji GB, Xu ZC (2019) A flexible microwave shield with tunable frequency-transmission and electromagnetic compatibility. Adv Funct Mater 29:1900163
5. Zhou XF, Jia ZR, Zhang XX, Wang BB, Liu XH, Xu BH, Bi L, Wu GL (2021) Electromagnetic wave absorption performance of $NiCo_2X_4$ (X=O, S, Se, Te) spinel structures. Chem Eng J 420:129907
6. Kong MY, Jia ZR, Wang BB, Dou JL, Liu XH, Dong YH, Xu BH, Wu GL (2020) Construction of metal-organic framework derived Co/ZnO/$Ti_3C_2T_x$ composites for excellent microwave absorption. Sustain Mater Techno 26:e00219
7. Zhang F, Jia ZR, Wang Z, Zhang CH, Wang BB, Xu BH, Liu XH, Wu GL (2021) Tailoring nanoparticles composites derived from metal-organic framework as electromagnetic wave absorber. Mater Today Phys 20: 100475.
8. Hou TQ, Jia ZR, Wang BB, Li HB, Liu XH, Bi L, Wu GL (2021) MXene-based accordion 2D hybrid structure with Co_9S_8/C/$Ti_3C_2T_x$ as efficient electromagnetic wave absorber. Chem Eng J 414:128875
9. Liang CB, Qiu H, Song P, Shi XT, Kong J, Gu JW (2020) Ultralight MXene aerogel/wood-derived porous carbon composites with wall-like "mortar/brick" structures for electromagnetic interference shielding. Sci Bull 65:616–622
10. Hou TQ, Jia ZR, Wang BB, Li HB, Liu XH, Chi QG, Wu GL (2021) Metal-organic framework derived $NiSe_2$-$CoSe_2$@C/$Ti_3C_2T_x$ composites as electromagnetic wave absorbers. Chem Eng J 422:130079
11. Wang YQ, Xie WH, Liu H, Gu HB (2020) Hyperelastic magnetic reduced graphene oxide three-dimensional framework with superb oil and organic solvent adsorption capability. Advanced Composites and Hybrid Materials 3:473–484
12. Jia ZR, Gao ZG, Kou KC, Feng AL, Zhang CH, Xu BH, Wu GL (2020) Facile synthesis of hierarchical A-site cation deficiency perovskite La_xFeO_{3-y}/RGO for high efficiency microwave absorption. Compos Commun 20:100344
13. Cui J, Chen X, Zhou Z, Zuo M, Xiao Y, Zhao N, Shi C, Guo X (2021) Effect of continuous pressures on electrochemical performance of Si anodes. Mater Today Energy 20:100632
14. Liang CB, Song P, Ma AJ, Shi XT, Gu HB, Wang L, Qiu H, Kong J, Gu JW (2019) Highly oriented three-dimensional structures of Fe_3O_4 decorated CNTs/reduced graphene oxide foam/epoxy nanocomposites against electromagnetic pollution. Compos Sci Technol 181:107683
15. Liu JL, Liang HS, Zhang Y, Wu GL, Wu HJ (2019) Facile synthesis of ellipsoid-like $MgCo_2O_4$/Co_3O_4 composites for strong wideband microwave absorption application. Compos Part B-Eng 176:107240
16. Zhao J, Zhang JL, Wang L, Li JK, Feng T, Fan JC, Chen LX, Gu JW (2020) Superior wave-absorbing performances of silicone rubber composites via introducing covalently bonded SnO_2@MWCNT absorbent with encapsulation structure. Compos Commun 22:100486
17. Zhang C, Long C, Yin S, Song RG, Zhang BH, Zhang JW, He DP, Cheng Q (2021) Graphene-based anisotropic polarization meta-filter. Mater Design 206:109768
18. Zhou XF, Jia ZR, Zhang XX, Wang BB, Wu W, Liu XH, Xu BH, Wu GL (2021) Controllable synthesis of Ni/NiO@porous carbon hybrid composites towards remarkable electromagnetic wave absorption and wide absorption bandwidth. J Mater Sci Technol 87:120–132
19. Xu XJ, Fu QG, Gu HB, Guo Y, Zhou H, Zhang JX, Pan D, Wu SD, Dong MY, Guo ZH (2021) Polyaniline crystalline nanostructures dependent negative permittivity metamaterials. Polymer 188:122129
20. Zhang HX, Jia ZR, Wang BB, Wu XM, Sun T, Liu XH, Bi L, Wu GL (2021) Construction of remarkable electromagnetic wave absorber from heterogeneous structure of Co-$CoFe_2O_4$@mesoporous hollow carbon spheres. Chem Eng J 421:129960
21. He SS, Jiang X, Li SW, Ran FT, Long J, Shao L (2020) Intermediate thermal manipulation of polymers of intrinsic microporous (PIMs) membranes for gas separations. AIChE J 66:e16543
22. Gao XR, Jia ZR, Wang BB, Wu XM, Sun T, Liu XH, Chi QG, Wu GL (2021) Synthesis of NiCo-LDH/MXene hybrids with abundant heterojunction surfaces as a lightweight electromagnetic wave absorber. Chem Eng J 419:130019
23. Guo J, Bao HF, Zhang YQ, Shen X, Kim JK, Ma J, Shao L (2021) Unravelling intercalation-regulated nanoconfinement for durably ultrafast sieving graphene oxide membranes. J Membrane Sci 619:118791
24. Lv HL, Yang ZH, Liu B, Wu GL, Lou ZC, Fei B, Wu RB (2021) A flexible electromagnetic wave-electricity harvester. Nat Commun 12:834
25. Zhang C, Sheng Y, Long C, Dong BW, He DP, Cheng Q (2021) Hybrid metamaterial absorber for ultra-low and dual-broadband absorption. Opt Express 29:14078–14086
26. Cai JY, Wang WX, Xie WC, Wei X, Liu H, Wei SY, Gu HB, Guo ZH (2020) Carbon microfibers with tailored surface functionalities supporting iron/nickel bisalloy for highly efficient hexavalent chromium recovery. Carbon 168:640–649
27. Zhou XF, Jia ZR, Feng AL, Wang KK, Liu XH, Chen L, Cao HJ, Wu GL (2020) Dependency of tunable electromagnetic wave absorption performance on morphology-controlled 3D porous carbon fabricated by biomass. Compos Commun 21:100404
28. Wang L, Shi XT, Zhang JL, Zhang YL, Gu JW (2020) Lightweight and robust rGO/sugarcane derived hybrid carbon foams with outstanding EMI shielding performance. J Mater Sci Technol 52:119–126

29. Lv HL, Yang ZH, Wang PL, Ji GB, Song JZ, Zheng LR, Zeng HB, Xu ZC (2018) A voltage-boosting strategy enabling a low-frequency, flexible electromagnetic wave absorption device. Adv Mater 30:1706343
30. Zhao HQ, Cheng Y, Lv HL, Ji GB, Du YW (2019) A novel hierarchically porous magnetic carbon derived from biomass for strong lightweight microwave absorption. Carbon 142:245–253
31. Huang L, Li JJ, Wang ZJ, Li YB, He XD, Yuan Y (2019) Microwave absorption enhancement of porous C@$CoFe_2O_4$ nanocomposites derived from eggshell membrane. Carbon 143:507–516
32. Qiu X, Wang LX, Zhu HL, Guan YK, Zhang QT (2017) Lightweight and efficient microwave absorbing materials based on walnut shell-derived nano-porous carbon. Nanoscale 9:7408–7418
33. Wu ZC, Tian K, Huang T, Hu W, Xie FF, Wang JJ, Su MX, Li L (2018) Hierarchically porous carbons derived from biomasses with excellent microwave absorption performance. ACS Appl Mater Interfaces 10:11108–11115
34. Zhou XF, Jia ZR, Feng AL, Kou JH, Cao HJ, Liu XH, Wu GL (2020) Construction of multiple electromagnetic loss mechanism for enhanced electromagnetic absorption performance of fish scale-derived biomass absorber. Compos Part B-Eng 192:107980
35. Lv HL, Yang ZH, Xu HB, Wang LY, Wu RB (2020) An electrical switch-driven flexible electromagnetic absorber. Adv Funct Mater 30:1907251
36. Lou ZC, Li R, Wang QY, Zhang Y, Li YJ (2021) Used dye adsorbent derived N-doped magnetic carbon foam with enhanced electromagnetic wave absorption performance. J Alloy Compd 854:157286
37. Wu GL, Jia ZR, Zhou XF, Nie GZ, Lv HL (2020) Interlayer controllable of hierarchical MWCNTs@C@Fe_xO_y cross-linked composite with wideband electromagnetic absorption performance. Compos Part A-Appl S 128:105687
38. Yang XT, Zhu JH, Yang D, Zhang JL, Guo YQ, Zhong X, Kong J, Gu JW (2020) High-efficiency improvement of thermal conductivities for epoxy composites from synthesized liquid crystal epoxy followed by doping BN fillers. Compos Part B-Eng 185:107784
39. Gao ZG, Jia ZR, Wang KK, Liu XH, Bi L, Wu GL (2020) Simultaneous enhancement of recoverable energy density and efficiency of lead-free relaxor-ferroelectric BNT-based ceramics. Chem Eng J 402:125951
40. Wang ZD, Meng GD, Wang LL, Tian LL, Chen SY, Wu GL, Kong B, Cheng YH (2021) Simultaneously enhanced dielectric properties and through-plane thermal conductivity of epoxy composites with alumina and boron nitride nanosheets. Sci Rep-UK 11:2495
41. Zhang C, Cao WK, Wu LT, Ke JC, Jing Y, Cui TJ, Cheng Q (2021) A reconfigurable active acoustic metalens. Appl Phys Lett 118:133502
42. Corma A, Atienzar P, Garcia H, Chane JY (2004) Hierarchically mesostructured doped CeO_2 with potential for solar-cell use. Nat Mater 3:394–397
43. Hao SY, Hou J, Aprea P, Pepe F (2014) Mesoporous CePrO solid solution with efficient photocatalytic activity under weak daylight irradiation. Appl Catal B- Environ 160–161:566–573
44. Xing HL, Yin Q, Liu ZF, Wang L (2017) Excellent microwave absorption behaviors of polyaniline composites containing CeO_2 nanorods in the X-Band. NANO 12:1750047
45. Shen ZY, Xing HL, Wang H, Jia HX, Liu Y, Chen AJ, Yang PY (2018) Synthesis and enhanced electromagnetic absorption properties of Co-doped CeO_2/RGO nanocomposites. J Alloy Compd 753:28–34
46. Wang ZQ, Zhao PF, He DN, Cheng Y, Liao LS, Li SD, Luo YY, Peng Z, Li PW (2018) Cerium oxide immobilized reduced graphene oxide hybrids with excellent microwave absorbing performance. Phys Chem Chem Phys 20:14155–14165
47. Wang ZQ, Zhao PF, Li PW, Li SD, Liao LS, Luo YY, Peng Z, He DN, Cheng Y (2019) Hierarchical cerium oxide anchored multi-walled carbon nanotube hybrid with synergistic effect for microwave attenuation. Compos Part B-Eng 167:477–486
48. Li QQ, Zhao YH, Li XH, Wang L, Li X, Zhang J, Che RC (2020) MOF induces 2D GO to assemble into 3D accordion-like composites for tunable and optimized microwave absorption performance. Small 16:2003905
49. Li QQ, Zhao YH, Wang L, Zhang J, Li X, Che RC (2020) 3D conductive network wrapped CeO_{2-x} Yolk@Shell hybrid microspheres for selective-frequency microwave absorption. Carbon 162:86–94
50. Li QQ, Liu JW, Zhao YH, Zhao XB, You WB, Li X, Che RC (2018) "Matryoshka doll"-like CeO_2 microspheres with hierarchical structure to achieve significantly enhanced microwave absorption performance. ACS Appl Mater Interfaces 10:27540–27547
51. Zhang XZ, Guo Y, Rashad A, Tian W, Liu YF, Zhang L, Wang X, Zhang LB, Yin LJ, Su H (2020) Bifunctional carbon-encapsulated FeSiAl hybrid flakes for enhanced microwave absorption properties and analysis of corrosion resistance. J Alloy Compd 828:154079
52. Guo Y, Jian X, Zhang L, Mu CH, Yin LJ, Xie JL, Mahmood N, Dou SX, Che RC (2020) Plasma-induced FeSiAl@Al_2O_3@SiO_2 core-shell structure for exceptional microwave absorption and anti-oxidation at high temperature. Chem Eng J 384:123371
53. Wang SJ, Li DS, Zhou Y, Jiang L (2020) Hierarchical $Ti_3C_2T_x$ MXene/Ni Chain/ZnO array hybrid nanostructures on cotton fabric for durable self-cleaning and enhanced microwave absorption. ACS Nano 14:8634–8645
54. Zhang JJ, Li ZH, Qi XS, Gong X, Xie R, Deng CY, Zhong W, Du YW (2021) Constructing flower-like core@shell $MoSe_2$-based nanocomposites as a novel and high-efficient microwave absorber. Compos Part B-Eng 222:109067
55. Yin Q, Xing HL, Shu RW, Ji XL, Tan DX, Gan Y (2016) Enhanced microwave absorption properties of CeO_2 nanoparticles supported on reduced graphene oxide. NANO 11:1650058
56. Jia ZR, Gao ZG, Feng AL, Zhang Y, Zhang CH, Nie GZ, Wang KK, Wu GL (2019) Laminated microwave absorbers of A-site cation deficiency perovskite $La_{0.8}FeO_3$ doped at hybrid RGO carbon. Compos Part B-Eng 176:107246
57. Xia W, Zhao J, Wang T, Song L, Gong H, Guo H, Gao B, Fan XL, He JP (2017) Anchoring ceria nanoparticles on graphene oxide and their radical scavenge properties under gamma irradiation environment. Phys Chem Chem Phys 19:16785–16794
58. Liu ZN, Zhao NQ, Shi CS, He F, Liu EZ, He CN (2019) Synthesis of three-dimensional carbon networks decorated with Fe_3O_4 nanoparticles as lightweight and broadband electromagnetic wave absorber. J Alloy Compd 776:691–701
59. Feng AL, Hou TQ, Jia ZR, Zhang Y, Zhang F, Wu GL (2020) Preparation and characterization of epoxy resin filled with $Ti_3C_2T_x$ MXene nanosheets with excellent electric conductivity. Nanomaterials 10:162
60. Qiao J, Zhang X, Xu DM, Kong LX, Lv LF, Yang F, Wang FL, Liu W, Liu JR (2020) Design and synthesis of TiO_2/Co/carbon nanofibers with tunable and efficient electromagnetic absorption. Chem Eng J 380:122591
61. Zhou XF, Wang BB, Jia ZR, Zhang XD, Liu XH, Wang KK, Xu BH, Wu GL (2021) Dielectric behavior of Fe_3N@C composites with green synthesis and their remarkable electromagnetic wave absorption performance. J Colloid Inter Sci 582:515–525
62. Liu PB, Gao S, Wang Y, Huang Y, Wang Y, Luo JH (2019) Core-Shell CoNi@Graphitic carbon decorated on B, N-Co doped hollow carbon polyhedrons toward lightweight and high-efficiency microwave attenuation. ACS Appl Mater Interfaces 11:25624–25635
63. Meng FB, Wang HG, Chen ZJ, Li T, Li CY, Xuan Y, Zhou ZW (2018) Generation of graphene-based aerogel microspheres for broadband and tunable high-performance microwave absorption by electrospinning-freeze drying process. Nano Res 11:2847–2861

64. Liu PB, Gao S, Wang Y, Huang Y, He WJ, Huang WH, Luo JH (2020) Carbon nanocages with N-doped carbon inner shell and Co/N-doped carbon outer shell as electromagnetic wave absorption materials. Chem Eng J 381:122653
65. Fan GH, Jiang YL, Hou CX, Deng XR, Liu ZX, Zhang LJ, Zhang ZD, Fan RH (2020) Extremely facile and green synthesis of magnetic carbon composites drawn from natural bulrush for electromagnetic wave absorbing. J Alloy Compd 835:155345
66. Zhang YH, Meng HJ, Shi YP, Zhang XF, Liu CX, Wang Y, Gong CH, Zhang JW (2020) TiN/Ni/C ternary composites with expanded heterogeneous interfaces for efficient microwave absorption. Compos Part B-Eng 193:108028
67. Nan HY, Qing YC, Gao H, Jia HY, Luo F, Zhou WC (2019) Synchronously oriented Fe microfiber & flake carbonyl iron/epoxy composites with improved microwave absorption and lightweight feature. Compos Sci Technol 184:107882
68. Wang R, Yang EQ, Qi XS, Xie R, Qin SJ, Deng CY, Zhong W (2020) Constructing and optimizing core@shell structure CNTs@MoS_2 nanocomposites as outstanding microwave absorbers. Appl Surf Sci 516:146159
69. Wu M, Darboe AK, Qi XS, Xie R, Qin SJ, Deng CY, Wu GL, Zhong W (2020) Optimization, selective and efficient production of CNTs/$Co_xFe_{3-x}O_4$ core/shell nanocomposites as outstanding microwave absorbers. J Mater Chem C 8:11936–11949
70. Ruan KP, Guo YQ, Lu CY, Shi XT, Ma TB, Zhang YL, Kong J, Gu JW (2021) Significant reduction of interfacial thermal resistance and phonon scattering in graphene/polyimide thermally conductive composite films for thermal management. Research 2021: 8438614